Local polarization switching in the presence of surface-charged defects: Microscopic mechanisms and piezoresponse force spectroscopy observations

Anna N. Morozovska* and Sergei V. Svechnikov
Institute of Semiconductor Physics, National Academy of Science of Ukraine, 45, Prospekt Nauki, 03028 Kiev, Ukraine

Eugene A. Eliseev
Institute for Problems of Materials Science, National Academy of Science of Ukraine, 3 Krjijanovskogo, 03142 Kiev, Ukraine

Brian J. Rodriguez, Stephen Jesse, and Sergei V. Kalinin†
Materials Science and Technology Division and Center for Nanophase Materials Science, Oak Ridge National Laboratory, Oak Ridge, Tennessee 37831, USA

(Received 9 November 2007; revised manuscript received 9 April 2008; published 4 August 2008)

Thermodynamic description of probe-induced polarization switching in ferroelectrics in the presence of well-localized surface field defects and their effect on local piezoresponse force spectroscopy measurements is analyzed. Corresponding analytical expressions for the free energy, activation energy, nucleation bias, and nucleus sizes are derived. Both numerical calculations and analytical expressions demonstrate that well-localized field defects significantly affect domain nucleation conditions. The signature of the defects in reproducible piezoresponse hysteresis loop fine structure are identified and compared to experimental observations. Deconvolution of piezoresponse force spectroscopy measurements to extract relevant defect parameters is demonstrated. Proposed approach can be extended to switching in other ferroics, establishing a pathway for the understanding of the thermodynamics and kinetics of phase transitions at a single-defect level.

DOI: 10.1103/PhysRevB.78.054101 PACS number(s): 64.60.Q−, 77.80.Dj

I. INTRODUCTION

Order parameter dynamics in ferroic materials, martensitic and disruptive phase transitions, and chemical reactions involving solid reagents are strongly mediated by the presence of defects.[1–3] In ferroelectric materials, a bias-induced transition between two equivalent polarization states (180° switching) is reversible and is not associated with diffusion, mass transport, significant heat exchange, and strain effects. Combined with the atomic-scale width of the ferroelectric domain wall, this enables applications such as nonvolatile random access memories,[4,5] ferroelectric tunnel junctions,[6,7] and high-density data storage.[8] Furthermore, electric-field induced polarization switching in ferroelectrics provides a convenient model system for more complex electrochemical processes. These considerations necessitate quantitative understanding of polarization switching in nanoscale volumes, and the role of local defects (or their absence) on the thermodynamics and kinetics of the switching process.

Ferroelectric and multiferroic films and crystals contain a range of point and extended defects in the bulk, at surfaces and interfaces. The role of defects on kinetics and thermodynamics of polarization switching is threefold. Defects can determine local phase stability (e.g., shift the Curie temperature),[9–11] act as nucleation centers in-phase transitions, and act as pinning centers for moving transformation fronts. The collective role of defects on these processes has been extensively studied for the last 50 yrs. The defect contribution to the thermodynamic properties can be analyzed on a statistically averaged level.[1] On the macroscopic level, the spatial and energy distributions of nucleation sites are a central element of Kolmogorov-Avrami[12,13] type theories of phase transitions.[14,15] Finally, the role of defects on domain-wall dynamics was addressed in a number of recent studies,[16] uncovering the plethora of emergent behaviors such as dynamic phase and depinning transitions.

Complementary to these *macroscopic* models, phase stability, domain-wall pinning, and domain nucleation can be studied *locally* on a single-defect level.[2] The role of defects on ferroelectric polarization switching in homogeneous electric field has been recognized since the seminal work by Landauer[17] 50 yrs ago, stimulating half a century long effort to identify the defect types that affect switching and pinning (see, e.g., Refs. 18–21). Recent experimental studies by Grigoriev *et al.*,[22] using ultrafast focused x-ray imaging, and Gruverman *et al.*[23] and Kim *et al.*[24] using piezoresponse force microscopy (PFM) has demonstrated that in the uniform field created in ~100 micron capacitor structures, the switching is initiated in very few (~1–10) locations and then propagates through the macroscopic (~10 s of microns) region of the electroded film. While the process is reproducible and the defect locations can be determined repeatedly, their identity and the energetic parameters of the nucleation process are unknown.

As a complementary approach to capacitor-based studies, switching in a nonuniform field of a scanning probe microscope has been studied by several groups. Landauer[17] model of the prolate semiellipsoidal domain formation in an ideal ferroelectric material was adapted for tip-induced switching by Molotskii and co-workers.[25,26] Recently this approach was significantly extended by taking into account a finite tip size and different surface screening conditions to determine the critical parameters of nucleation process.[27]

Overall, despite the significant effort on studies of domain switching mechanisms in ferroelectrics, the key element required for linking macroscopic statistical theories and probe

microscopy experimental studies—the influence of a single-defect center on thermodynamics of the nanoscale polarization reversal in the highly localized electric field produced by the tip—is missing.

Here we develop the thermodynamical description of the probe-induced nucleation process in the vicinity of well-separated surface field defects, relating the probe-induced phase transition to defect properties. Furthermore, we calculate the signature of local defect on piezoresponse force spectroscopy (PFS) measurements. This paper is organized as follows. Section II provides a brief overview of piezoresponse force microscopy and spectroscopy. The thermodynamics of defect-mediated phase transition, and relationship between nascent domain size and PFM signal is developed in Sec. III for arbitrary defect and domain geometry. Section IV summarizes the analytical results developed for the case of surface field defect, as suggested by Guerra and Tagantsev.[21] Finally, Sec. V illustrates representative experimental studies of point-defect spectroscopy. This analysis lays the foundation for local studies of defect effects on phase transitions at a single-defect level.

II. PIEZORESPONSE FORCE MICROSCOPY STUDIES OF DOMAIN-DEFECT LOCAL INTERACTIONS

A significant insight into local switching processes in ferroelectrics was achieved with the invention of PFM imaging, domain patterning, and spectroscopy. In PFM, the probe concentrates an electric field to a nanoscale volume of material ($\sim$10–50 nm), and induces local domain nucleation and growth (bias-induced *local phase transition*). The size of the created domain as a function of length and duration of the switching pulse is imaged, providing information of switching process. Recent studies by Ramesh and co-workers,[28,29] Agronin *et al.*,[30] Kholkin *et al.*,[31] and Woo *et al.*[32] demonstrate the scaling laws for bias-induced domain growth. These studies allow direct imaging of domain growth but are extremely time consuming ($\sim$10 s hours/location). Complementary to these are the studies by Shvartsman and Kholkin,[33] and Likodimos and co-workers[34,35] based on the statistical analysis of the domain patterns and domain-wall roughness, which provide the information on the collective effect of defect centers on the switching process.

In contrast to the direct imaging studies, switching dc bias and probing ac bias are applied to the tip simultaneously in PFM spectroscopy, offering the advantage of larger bandwidth ($\sim$1 s/spectrum). Resulting local electromechanical hysteresis loop contains information on local switching, specifically domain size-voltage dependence. In particular, recent studies illustrate that PFS hysteresis loops often possess fine structure that can be interpreted as the interaction between growing domain and adjacent defect.[36–38] Such "non-ideal" loop shape can be noticed on many published examples of PFM spectroscopy. The work of Abplanalp *et al.*[39] and Harnagea *et al.*[40] attribute anomalous loop shapes to high-order switching and spatial confinement effects, respectively. An extensive number of anomalous loops were collected in work by Buhlmann.[41] The first interpretation of anomalous loop shape as due to domain-ferroelastic wall interaction was published by Le Rhun and co-workers,[36,42] and Jesse and co-workers.[43,44]

The significant advantage of the spectroscopic studies is that hysteresis loops can be measured at a finely spaced grid of locations on sample surface (since process is *reversible*, unlike, e.g., nanoindentation). In this manner, the switching can be probed at different separation from known or unknown defect, allowing to study defect role on switching systematically (e.g., by varying tip-defect separation). Correspondingly, imaging and spectroscopic studies of domain-defect interactions require both the signatures of the defect on local spectroscopic data to be established, and quantitative relationship between the defect parameters and the measured signal to be developed.

III. GENERAL APPROACH AND PROBLEM STATEMENT

Defects in ferroelectric materials are associated with the disruption in lattice periodicity and associated changes in electronic structure. Local charge redistribution in the defect core is compensated by local band bending and Debye screening, leading to the exponential vanishing of Coulomb electric fields away from the localized defect. Far from structurally distorted defect core, the electric field couples linearly to the polarization order parameter, stabilizing preferential polarization states. Therefore, the natural choice for defect model in ferroelectric material is the random-field defect, as analyzed by Gerra *et al.*[21] The choice of electric field, rather than charge or elastic stress distribution, as a defect model is motivated by (a) the fact that field, rather than charge, linearly couples to the polarization, (b) the field-distribution models are less sensitive to the exact atomic and electronic structures of the defect, and (c) evident analytical expressions for free energy cannot be obtained for localized elastic defects.

A. Problem statement

We assume that the defect causes the built-in electric field[21] that directly couples to polarization (random field). The analysis of the switching process thermodynamics is simplified for a rigid piezoelectric, for which effective material constants are independent of the electric field. The surface and electrostatic energies of the semiellipsoidal domain in semi-infinite ferroelectric material is

$$\Phi(\mathbf{r},U)=\Phi_S(\mathbf{r})+\Phi_D(\mathbf{r})+\Phi_P(\mathbf{r},U)+\Phi_d(\mathbf{r}), \tag{1}$$

where the surface, depolarization, tip-induced, and defect contributions to free energy are

$$\Phi_S(\mathbf{r})=\psi_S S, \tag{2a}$$

$$\Phi_D(\mathbf{r})=\frac{n_D}{\varepsilon_0\varepsilon_{11}}P_S^2V, \tag{2b}$$

$$\Phi_P(\mathbf{r},U)=-2P_S\int_V d^3x\cdot E_3^p(\mathbf{x}), \tag{2c}$$

$$\Phi_d(\mathbf{r}) = -2P_S \int_V d^3x \cdot E_3^d(\mathbf{x}). \tag{2d}$$

S and V are the domain surface and volume, ψ_S is the domain-wall energy density, and P_s is the magnitude of material spontaneous polarization $\mathbf{P}=(0,0,P_S)$. Depolarization field energy is calculated under the condition of perfect tip-surface electric contact and/or surface screening by free charges. Rigorous expression for the depolarization factor n_D is given in Ref. 45. Electric field established by the probe is $\mathbf{E}^p(\mathbf{x})=-\nabla\varphi_p(\mathbf{x})$, and electric field created by the defects is $\mathbf{E}^d(\mathbf{x})=-\nabla\varphi_d(\mathbf{x})$. U is the electric bias applied to the PFM probe; vector $\mathbf{r}$ describes the domain geometry (e.g., sizes and position).

Typical energy barriers for the polarization switching in perfect ferroelectric materials well below Curie temperature are much higher than thermal fluctuations (e.g., barrier is much greater than $\sim 10^3 k_B T$ for the plain electrode geometry). Hence, the thermal disorder is anticipated to be negligibly small and the equilibrium domain growth will proceed along the lowest free-energy path on the free-energy surface given by Eq. (1). This is in agreement with high reproducibility of fine structure between the loops.[37] The switching process can then be analyzed from the bias-dependent geometry of $\Phi(\mathbf{r},U)$ surface.

Stable domain configurations correspond to local minima on the $\Phi(\mathbf{r},U)$ surface. In the case of first-order phase transitions, the minima and coordinate origin are separated by saddle points. The saddle-point-metastable minimum pair appears at voltage, U_s. The minimum becomes stable (i.e., $\Phi(\mathbf{r},U)<0$) at the critical voltage, U_{cr}. Numerically, for most ferroelectric materials for typical tip parameters, U_S is close to U_{cr}. The free-energy value in the saddle point determines the activation energy, E_a, of domain nucleation. The relaxation time necessary for the stable domain formation at U_{cr} is maximal and the critical slowing down appears in accordance with general theory of phase transitions. Within the framework of activation rate theory, the domain nucleation takes place at higher activation voltage U_a determined from the condition $\Phi(U_a)=E_a$, corresponding to the activation time $\tau=\tau_0 \exp(E_a/k_BT)$. For instance, the activation energy $E_a=20k_BT$ corresponds to a relatively fast nucleation time $\tau\sim 10^{-3}$ s for phonon relaxation time $\tau_0=10^{-12}$ s while the condition $E_a\leq 2k_BT$ corresponds to "instant" or thermal nucleation.

The difference between the voltages corresponding to the formation of a saddle point and a stable domain, U_s-U_{cr}, determines the width of the (rather thin) thermodynamic hysteresis loop. More realistic models of piezoresponse hysteresis loop formation consider domain-wall pinning effects. In the weak pinning limit, the domain growth in the forward direction is assumed to follow the thermodynamic energy minimum while on decreasing bias, the domain remains stationary due to domain-wall pinning by the lattice and atomic defects.

Further analysis is performed, assuming that the domain possesses well-defined semiellipsoidal geometry, i.e., it has radius r and length l, but allowing for defect influence, its center is shifted on value y_0 compared to the tip location.

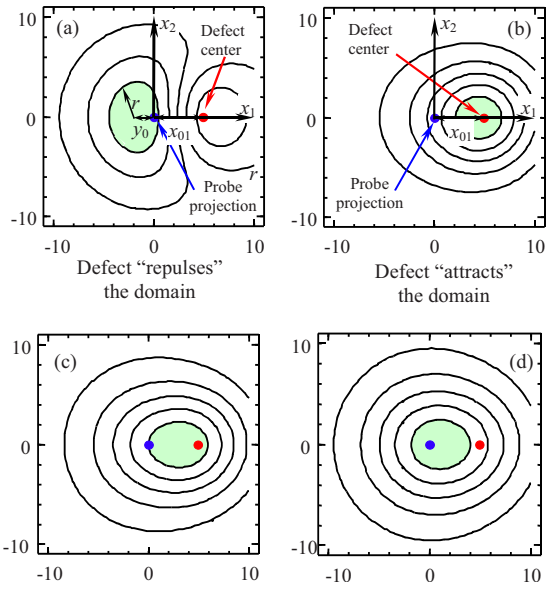

FIG. 1. (Color online) Schematics of domain nucleation in the vicinity of surface Gaussian field defect of radius $r_d=5$ nm and maximal field strength E_S located at distance $x_{01}=5$ nm from the biased at voltage U probe apex of characteristic size $d=8$ nm, $\gamma=1$. (a) $U=10$ V and $E_S=-1$ V/nm, (b) $U=3$ V and $E_S=1$ V/nm, (c) $U=10$ V and $E_S=1$ V/nm, and (d) $U=30$ V and $E_S=1$ V/nm. Contour lines correspond to the constant electric field. Domain nucleation appears inside the filled area with the highest field strength.

The domain center shift, y_0, is thus the parameter defining defect effect on tip-induced switching. The center of the nearest surface field defect is assumed to be located at position $\mathbf{x}_0=\{x_{10},0,0\}$, whereas the tip is located at the coordinate origin (see Fig. 1). Hereinafter, we consider the domain center displacement as a variational parameter.

Rigorously speaking, the domain shape will deviate from semiellipsoidal when $x_{01}\neq 0$ (the system radial symmetry is broken). However, analytical treatment of the problem necessitates a limit on the number of free parameters describing geometry and development of analytical theory requires no more then three independent parameters (e.g., domain center shift or general ellipsoid shape of the domain). Additional numerical calculations proved that the choice of domain shift, as an optimal variation parameter, works surprisingly well for domain nucleation in the presence of well-localized rotationally symmetric field defect. For instance, domain nucleation appears inside the filled area shown in Fig. 1 since the field strength is highest here. Because isopotential line shape is almost axisymmetric inside the filled area, the nucleus shape can be expected to be close to axisymmetric as well. This reflects the well-known behavior of the isopotential lines in the system of two point charges. Moreover, experimental data[31] proved that deviations of equilibrium domain shape from the radial symmetry are small even in nanograined ceramics, which contained numerous surface defects.

B. Domain-probe and domain-defect interaction energies

For transversally isotropic material and a rotationally symmetric probe, corresponding to the prototype case of

switching in tetragonal and hexagonal ferroelectrics, the probe electric potential, $\varphi_p(\mathbf{x})$, is an axially symmetric even function. Hence, $\varphi_p(\mathbf{x}) \equiv \varphi_p(\rho, x_3)$, where $\sqrt{x_1^2+x_2^2}=\rho$ and x_3 are the radial and vertical coordinates, respectively. In this case, the domain-tip interaction energy $\Phi_p(r,l,y_0)$ can be rewritten as

$$\Phi_p(r,l,y_0) = 2P_S \int_0^l dx_3 \int_0^{2\pi} d\varphi \int_0^{r\sqrt{1-x_3^2/l^2}} \rho d\rho E_3^p \times (\sqrt{\rho^2 + y_0^2 + 2\rho y_0 \cos\varphi}, x_3). \quad (3)$$

The flattened or spherical probe potential φ_p can be modeled using an effective point-charge approximation. The probe is represented by a single charge Q located at distance d from a sample surface (see details in Ref. 46). The potential φ_p at $x_3 \geq 0$ has the form

$$\varphi_p(\rho, x_3) \approx \frac{Ud}{\sqrt{\rho^2 + (x_3/\gamma + d)^2}}. \quad (4)$$

Here $\gamma=\sqrt{\varepsilon_{33}/\varepsilon_{11}}$ is the dielectric anisotropy factor. In the case of local point-charge model, the probe is represented by a single charge $Q=2\pi\varepsilon_0\varepsilon_e R_0 U(\kappa+\varepsilon_e)/\kappa$ located at $d=\varepsilon_e R_0/\kappa$ for a spherical tip or $d=2R_0/\pi$ for a flattened tip represented by a disk in contact, where $\kappa=\sqrt{\varepsilon_{33}\varepsilon_{11}}$ is the effective dielectric constant.

Substituting potential Eq. (4) into Eq. (3) and performing the integration, we derive the Pade approximation for the tip-induced interaction energy for a shifted domain as

$$\Phi_p(r,l,y_0) \approx \frac{-4\pi U P_S d r^2 l/\gamma}{(\sqrt{r^2+d^2+y_0^2}+d)(\sqrt{r^2+d^2+y_0^2}+d+l/\gamma)}. \quad (5)$$

Assuming that the defect-induced built-in electric field can be represented as $E_3^d(\mathbf{x}) = E_3^d[\sqrt{(x_1-x_{01})^2+x_2^2}, x_3]$, i.e., it is rotationally symmetric with respect to the defect center, the domain-defect interaction energy can be rewritten via the overlap integral:

$$\Phi_d(r,l,x_{01}-y_0) = -2P_S \int_0^l dx_3 \int_0^{2\pi} d\varphi \int_0^{r\sqrt{1-x_3^2/l^2}} \rho d\rho E_3^d \times [\sqrt{\rho^2 + (x_{01}-y_0)^2 - 2\rho\cos\varphi(x_{01}-y_0)}, x_3]. \quad (6)$$

Equation (6) thus describes the defect contribution into the free energy of domain.

C. Effective piezoresponse calculations

Measured in a PFS experiment is the electromechanical response related to the size of ferroelectric domain formed below the tip. Hence, to calculate the shape of the PFM hysteresis loop, the electromechanical response change induced by the domain is required. A number of approximate solutions for PFM responses have been recently derived using decoupling approximations.[47–49] Here, we employ the same approach for calculation of PFM response from the domain of arbitrary geometry. Within the framework of linearized theory by Felten *et al.*,[50] the surface displacement vector $u_i(\mathbf{x})$ at position $\mathbf{x}$ is

$$u_i(\mathbf{x}) = \int_0^\infty d\xi_3 \int_{-\infty}^\infty d\xi_2 \int_{-\infty}^\infty d\xi_1 \frac{\partial G_{ij}(\mathbf{x},\boldsymbol{\xi})}{\partial \xi_l} E_k^p(\boldsymbol{\xi}) d_{kmn}(\boldsymbol{\xi}, r, l, y_0) \times c_{nmjl}, \quad (7)$$

where $\boldsymbol{\xi}$ is the coordinate system related to the material, d_{nmp} are strain piezoelectric coefficients distribution, c_{nmjl} are elastic stiffness and the Einstein summation convention is used, and E_k^p is the electric field created by the biased probe. For typical ferroelectric perovskites, the symmetry of the elastic properties can be approximated as cubic (anisotropy of elastic properties is much smaller than that of dielectric and piezoelectric properties) and therefore an isotropic approximation can be used for Green's function, $G_{ij}(\mathbf{x},\boldsymbol{\xi})$.[48,51]

Integration of Eq. (7) for $x_3=0, \rho=0$ yields the expression for effective vertical piezoresponse, $d_{33}^{\text{eff}}=u_3/U$, as

$$d_{33}^{\text{eff}}(r,l,y_0) = d_{31}g_1(r,l,y_0) + d_{15}g_2(r,l,y_0) + d_{33}g_3(r,l,y_0). \quad (8)$$

Functions $g_i(r,l,y_0)=f_i-2w_i(r,l,y_0)$, where $w_i=0$ in the initial and $w_i=f_i$ in the final state. The functions f_i are $f_1=-[2\nu(1+\gamma)+1]/(1+\gamma)^2$, $f_2=-\gamma^2/(1+\gamma)^2$, and $f_3=-(1+2\gamma)/(1+\gamma)^2$, where ν is the Poisson ratio, and define the electromechanical response in the initial and final states of switching process.[52] Considering the signal generation volume in PFM, piezoresponse changes negligibly when the domain is far from the tip, i.e., $|w_i| \ll |f_i|$ under the condition $|y_0| \gg r$. For the opposite case $|y_0| < r$, functions w_i have integral representations:

$$w_1(r,l,y_0) = \frac{1}{2\pi}\int_0^{2\pi} d\varphi \int_0^{\pi/2} d\theta [3\cos^2\theta - 2 \times (1+\nu)]\cos\theta \sin\theta \frac{R_w(\theta,\varphi,r,l,y_0)}{R_G(\theta,\varphi,r,l,y_0)}, \quad (9)$$

$$w_2(r,l,y_0) = \frac{3}{2\pi}\int_0^{2\pi} d\varphi \int_0^{\pi/2} d\theta \left[\frac{\gamma d + \cos\theta R_w(\theta,\varphi,r,l,y_0)}{R_G(\theta,\varphi,r,l,y_0)} - 1\right]\cos^2\theta \cdot \sin\theta, \quad (10)$$

$$w_3(r,l,y_0) = -\frac{3}{2\pi}\int_0^{2\pi} d\varphi \int_0^{\pi/2} \times d\theta \cos^3\theta \sin\theta \frac{R_w(\theta,\varphi,r,l,y_0)}{R_G(\theta,\varphi,r,l,y_0)}. \quad (11)$$

Here, the radius $R_w(\theta,\varphi,r,l,y_0)$ determines the domain-wall shape and its center position. In the typical case of prolate semiellipsoid ($r \ll l$) or cylinder, we derive

$$R_w(\theta,\varphi,r,y_0)=\frac{|y_0|\cos\varphi+\sqrt{r^2-y_0^2\sin^2\varphi}}{\sin\theta}. \quad (12a)$$

The function $1/R_G(\theta,\varphi,r,y_0)$ is related to the probe electrostatic potential in the domain-wall point determined by $R_w(\theta,\varphi,r,y_0)$, namely

$$R_G(\theta,\varphi,r,y_0)=\sqrt{[\gamma d+\cos\theta R_w(\theta,\varphi,r,y_0)]^2+\gamma^2\sin^2\theta R_w^2(\theta,\varphi,r,y_0)}. \quad (12b)$$

At $y_0=0$ (no lateral shift), expressions (9)–(11) coincide with the ones derived for domain nucleating on the tip axis in Ref. 27, as expected.

Using the approach proposed in Ref. 49 for $y_0=0$ and superposition principle of PFM signal calculations at $|y_0|\ll r$ [see Fig. 1(c)], we obtained Pade approximations for effective electromechanical response, $d_{33}^{\text{eff}}(r,y_0)$, as

$$d_{33}^{\text{eff}}(r,y_0)\approx\left\{\frac{3}{4}d_{33}^*\left[1-\frac{16r}{\pi d+8r}+\frac{8\pi d(\pi d+24r)}{r(\pi d+8r)^3}y_0^2\right]+\frac{d_{15}}{4}\left[1-\frac{16r}{3\pi d+8r}+\frac{24\pi d(3\pi d+24r)}{r(3\pi d+8r)^3}y_0^2\right]\right\}. \quad (13)$$

Here, the material is regarded dielectrically isotropic, $\gamma=1$, $r=r(U)$ is the voltage dependent domain radius, and $d_{33}^*=d_{33}+(1+4\nu)d_{31}/3$.

IV. SURFACE FIELD DEFECTS

A. Domain free energy affected by a surface field defect

Here we adopt a model of a laterally localized surface field defect with characteristic radius, r_d, and penetration depth, $h_d\ll r_d$, located at the point $\{x_{01},0,0\}$, for which the longitudinal component of electric field is

$$E_3^d(\mathbf{x})=E_S\exp\left[-\frac{(x-x_{01})^2+x_2^2}{r_d^2}-\frac{x_3}{h_d}\right]. \quad (14)$$

Corresponding charge distribution could be related with charge accommodation at the *vertical dislocation line* and *dislocation-surface junction* (see Appendix A), in agreement with expected behavior for threading dislocations in polar materials.[53] In the limit $|x_{01}-r_d|\gg d$, the tip is well-separated from the defect, and hence, the defect role on tip-induced switching is minimal. Therefore, here we analyze the switching behavior for $|x_{01}-r_d|\sim d$. Based on comparison with the critical nucleation domain size and switching fields, the relevant values of the penetration depth are $h_d\sim 1-2$ nm, maximal field strength $E_S=10^8-10^{10}$ V/m, and defect radius is $r_d\sim 1-50$ nm. For larger radius, the defect becomes significantly larger than PFM tip size, and hence, can be approximated by the homogeneous surface field considered in Ref. 21. Similarly, field strength below $\sim 10^8$ V/m is much smaller than the fields at tip-surface junction during the PFM experiment, and hence, the defect is unlikely to affect the nucleation process. Finally, the condition on penetration depth is chosen to correspond to surface field defect associated with surface structural defects.

Substituting defect-induced electric field from Eq. (14) into the domain free energy given by Eq. (2), we obtain

$$\Phi_S(r,l)=\pi\psi_S l r\left(\frac{r}{l}+\frac{\arcsin\sqrt{1-r^2/l^2}}{\sqrt{1-r^2/l^2}}\right), \quad (15a)$$

$$\Phi_D(\mathbf{r})=\frac{P_S^2}{\varepsilon_0\varepsilon_{33}}\frac{4\pi r^2 l}{3}\frac{(r\gamma/l)^2}{1-(r\gamma/l)^2}\left[\frac{\operatorname{arctanh}[\sqrt{1-(r\gamma/l)^2}]}{\sqrt{1-(r\gamma/l)^2}}-1\right], \quad (15b)$$

$$\Phi_P(r,l,y_0,U)=-\frac{4\pi U P_S d r^2 l/\gamma}{(\sqrt{r^2+d^2+y_0^2}+d)(\sqrt{r^2+d^2+y_0^2}+d+l/\gamma)}, \quad (15c)$$

$$\Phi_d(r,l,x_{01},y_0)=-2\pi r_d^2 h_d P_S E_S I_S(r,l,x_{01}-y_0). \quad (15d)$$

The dimensionless overlap integral $I_S(r,l,x)$ has the form

$$I_S(r,l,x)\approx\left[1-\exp\left(-\frac{l}{h_d}\right)\right]\left[1-\exp\left(-\frac{r^2}{r_d^2}\right)\right]\exp\left(-\frac{x^2}{r_d^2}\right). \quad (16)$$

After minimization of Eq. (15) with respect to the domain center shift toward the defect, y_0, the domain free energy can be represented as a two-dimensional (2D) surface in coordinates r and l. The nucleus size $\{r_S,l_S\}$, minimal critical domain size $\{r_{cr},l_{cr}\}$, and equilibrium size-voltage dependences $\{r(U),l(U)\}$ are found from the free-energy saddle point and minima, correspondingly.

To illustrate this behavior, below we compare the free-energy contour maps, activation barrier, critical voltage, and domain size that correspond to the states with different x_{01} (i.e., tip positioned at different separations from the defect).

1. Defect center below the probe apex

Even in the simplest case when the surface field defect is located just below the tip apex (i.e., $x_{01}=0$), the spatial distribution of the driving electric field is rather complex depending on the surface field amplitude, E_S, its sign, and half-width, r_d. On the sample surface, the total electric field can be written as $E_3(\rho,0)=U(\rho^2+d^2)^{-3/2}d^2/\gamma+E_S\exp(-\rho^2/r_d^2)$ and illustrated in Fig. 2(a).

A number of universal interesting behaviors can be predicted depending on the relative magnitude of tip-induced and defect-induced electric fields. For a positive surface field ($E_S>0$) and a positive tip bias ($U>0$), the field $E_3(\rho,0)$ is maximal just below the tip ($\rho=0$) and so the domain forms exactly at $y_0=x_{01}=0$ [see curves 1–3 in Fig. 2(a)]. For positive bias and negative surface defect of sufficient field strength, $E_S<-U/\gamma d$, the driving electric field $E_3(\rho,0)$ could be maximal on the ring $\rho=y_r\neq 0$ at $x_3=0$ [see Fig. 2(a), curves 5 and 6]. Thus every point of the ring is an equal-probable candidate for domain nucleation. For instance, the domain-tip-defect negative interaction energy $\Phi_d(r,l,y_0)+\Phi_p(r,l,y_0)$ depicted in Fig. 2(b) is minimal at

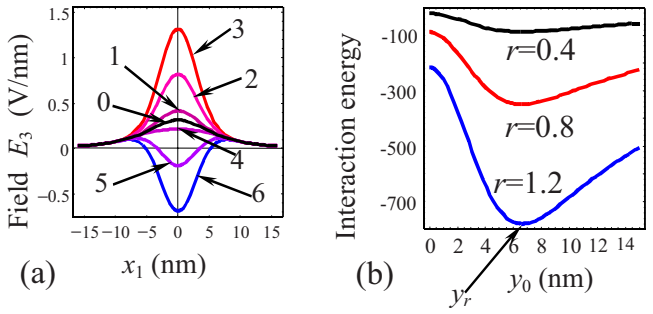

FIG. 2. (Color online) (a) Driving electric-field $E_3(\rho,0)$ distribution on the surface at applied voltage $U=2.5$ V. Surface field defect of radius $r_d=4$ nm, penetration depth $h_d=0.8$ nm, and amplitude $E_S=0;10^8;5\times10^8;10^9;-10^8;-5\times10^8;-10^9$ V/m (curves 0–6) is located below the tip apex ($x_{01}=0$). (b) Corresponding interaction energy via the shift y_0 for $E_S=-10^9$ V/m, $l=10$ nm, and different domain radius $r=0.4$, 0.8, and 1.2 nm (figures near the curves). Material parameters $P_S=0.5$ C/m^2 and $\gamma\approx1$; point-charge-surface separation $d=8$ nm.

$y_0\approx6$ and maximal at $y_0\approx0$ for nucleus radius and typical material parameters similar to those above [note that this behavior is a result of the different distance behavior of the field components, and hence, is nonuniversal]. However, for large enough biases (2–3 V for chosen material parameters), the interaction energy becomes minimal at $y_0\approx0$ with domain radius increasing up to 10–20 nm, indicating that the center of the stable semiellipsoidal domain with a radius of more than several r_d should be located below the tip. Thus, the lowest thermodynamic path of domain formation effected by the strong negative surface field defect located at $x_{01}\approx0$ is expected to start on the ring $\rho=y_r\neq0$ (nucleation stage) and then transforming into the stable domain with center at $y_0\approx0$.

Voltage-dependent free-energy surfaces defined by Eq. (15) in the presence of a surface field defect located directly below the tip apex ($x_{01}=0$) are shown in Fig. 3. The maps are calculated for PZT-6B ceramics [modified $Pb(Zr,Ti)O_3$ solid solution].

Shown in Fig. 3 are the cross section of $\Phi(r,l,y_0)$ in coordinates of domain radius, r, and length, l, at $y_0=0$. As shown above, the case $y_0=0$ is the nucleation site for voltages $U>-\gamma dE_S$ that corresponds to $U>8$ V for $E_S=-10^9$ V/m, and $U>-8$ V at $E_S=+10^9$ V/m for chosen materials and tip parameters. Thus the saddle points in parts (b)–(f) correspond to the lowest activation barrier, whereas the saddle shown in part (a) for $U=2.5$ V corresponds to the highest barrier. Shown in Fig. 3(a) is the saddle at $y_0=0$ corresponding to the barrier of $4200k_BT$. The lowest saddle (with activation energy $2600k_BT$) appeared at $y_0=8$ nm (not shown since it corresponds to the ringlike nucleus).

Similar to switching on a defect-free surface,[27] the activation barrier rapidly decreases with applied voltage. A favorable (positive) surface field defect decreases the activation barrier and thus stimulates domain nucleation at lower applied voltages [Figs. 3(d)–3(f)] in comparison with an unfavorable (negative) field defect [Figs. 3(a)–3(c)].

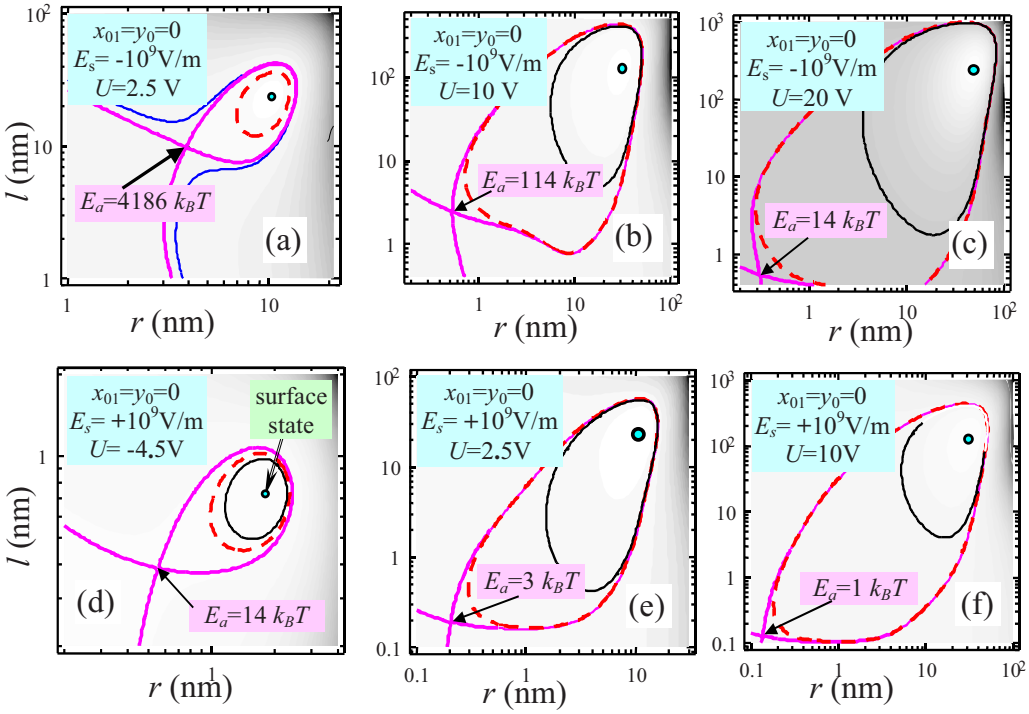

FIG. 3. (Color online) Voltage dependence of free-energy surfaces in the presence of surface field defect located below the tip apex ($x_{01}=0$) with radius $r_d=4$ nm, penetration depth $h_d=0.8$ nm, amplitude $E_S=-10^9$ V/m (parts a–c), and $E_S=+10^9$ V/m (parts d–f). Labels correspond to the domain shift y_0 in nanometer and activation energy values in k_BT units. Dashed contour corresponds to zero energy. Small circle and arrow with label denote absolute minimum (equilibrium domain sizes) and activation barrier E_a (saddle point and contour), correspondingly. Material parameters correspond to PZT-6B: $P_S=0.5$ C/m^2, $\varepsilon_{33}\approx500$, $\gamma\approx1$, and $\psi_S=150$ mJ/m^2; point-charge-surface separation $d=8$ nm corresponds to the local charge approximation for sphere-plane model of tip-surface contact.

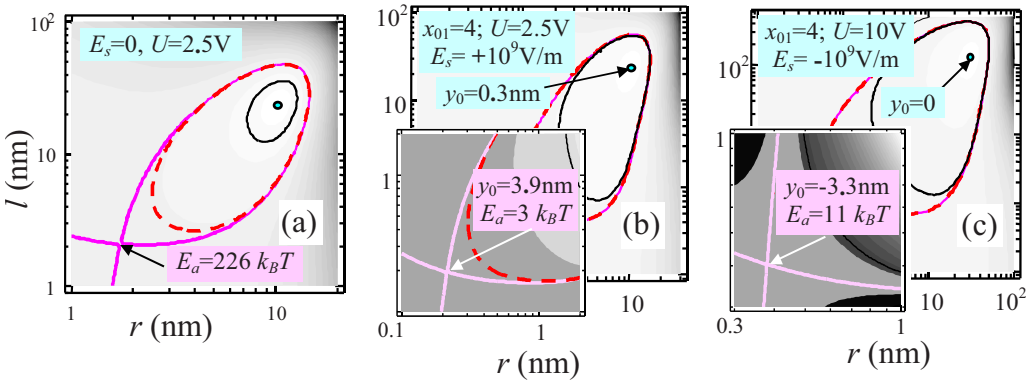

FIG. 4. (Color online) Voltage dependence of free-energy surfaces in the presence of surface field defect (r_d=4 nm and h_d=0.8 nm) for different distances x_{01} from the defect center and maximal field: (a) E_S=0; (b) x_{01}=4 nm, attracting positive defect with E_S=+10^9 V/m; and (c) x_{01}=4 nm, repulsing negative defect with E_S=−10^9 V/m. Dashed contour corresponds to zero energy. Arrow with label and small circle denote activation barrier E_a (saddle point and contour), and absolute minimum (stable domain), correspondingly. Material parameters and tip characteristics are the same as in Fig. 3.

Activation voltages (corresponding to the case when thermal nucleation is possible) are typically much greater than the critical ones (corresponding to the thermodynamic stability of the domains). For the chosen material parameters and a negative surface field ($E_S<0$), the critical voltage U_{cr}^-, determined from the condition $\Phi(U_{cr}^-)=0$ at minimum, is about 2 V, whereas the activation voltage U_a^-, determined from the condition $\Phi(U_a^-)\approx 20k_BT$ in a saddle point, is about 20 V [compare parts (a) and (c) of Fig. 4].

The favorable field defect ($E_S>0$) acts as a nucleation center at zero or even negative voltages [see, e.g., Figs. 3(d) and 3(e)]. The surface state (i.e., stable domain with length $l\cong h_d$, radius $r\leq r_d$, and center at $y_0=x_{01}$) appears when the defect field strength exceeds the critical value, E_S^{cr}, determined as (see Appendix B for details)

$$E_S^{cr}\approx\frac{2e}{3(e-1)}\left(\frac{\psi_S}{h_dP_S}+\frac{P_S}{\varepsilon_0\varepsilon_{11}}\right). \tag{17}$$

The surface state becomes unstable for a negative external field $E_0<-E_S^{cr}$. Experimentally, the surface state will correspond to a "frozen" polarization level for low enough fields.

2. Defect at the intermediate separation from the tip apex

The effect of domain attraction or repulsion by the surface field defect with the center located at different distances $x_{01}\neq 0$ from the probe apex is illustrated in Fig. 4. Numerical calculations show that positive field defects with sufficient electric-field strength, $E_S>E_S^{cr}$, located at distances $|x_{01}|\leq r_d$ always act as nucleation centers at voltages $U\geq 0$. During this process, $y_0\approx x_{01}$ in the saddle point and the positive difference $(x_{01}-y_0)$ slightly increases with applied voltage increase (see insets indicating defect-induced nucleation). Even at high voltage the domain position is centered at the defect. However, the equilibrium domain position is below the tip, i.e., $y_0\approx 0$ under the same conditions (see main plots indicating tip-induced growth). This analysis implies that the domain nucleates at the defect site ($y_0\approx x_{01}$ in the saddle point) and then evolves to its equilibrium location below the tip ($y_0\approx 0$) when the probe electric field substantially exceeds the defect field.

Negative defects with sufficient field strength located at distances $|x_{01}|\leq r_d$ always delay the nucleation [Figs. 4(c)], i.e., the domain nucleus repulses from the defect, $y_0\leq 0$ (see corresponding saddle points). Similarly to the case of positive field defect, the equilibrium thermodynamic domain position is below the tip (see main plots in Fig. 4).

The effect of domain attraction or repulsion by the surface field defect with center located at different distances x_{01} from the probe apex is numerically analyzed in Fig. 5. Corresponding defect-mediated domain nucleation and growth in thermodynamic and weak pinning limits are shown in Fig. 6. In thermodynamic limit, critical nucleus typically appears at the nearest favorable defect site, and rapidly grows and moves as a whole toward the probe apex [see Fig. 6(a)]. In the presence of the wall pinning by the lattice or point defect that prevents domain movement as a whole, domain can only grow and thus may acquire the bulb-like shape as shown in Figs. 6(b) and 6(d). Such morphology was observed by Kholkin *et al.*[31]

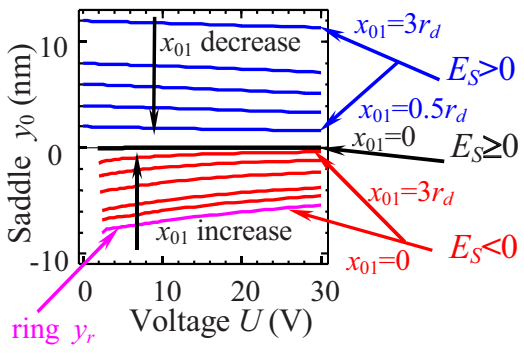

FIG. 5. (Color online) (a) Voltage dependence of the domain nucleus center shift y_0 at the saddle point for surface field defect of r_d=4 nm and h_d=0.8 nm, and field strength E_S=+10^9;0; −10^9 V/m (see right labels). Shown are curves for tip-defect separations x_{01}=12, 8, 6, 4, 2, and 0 nm. Material parameters and tip characteristics are the same as in Fig. 3.

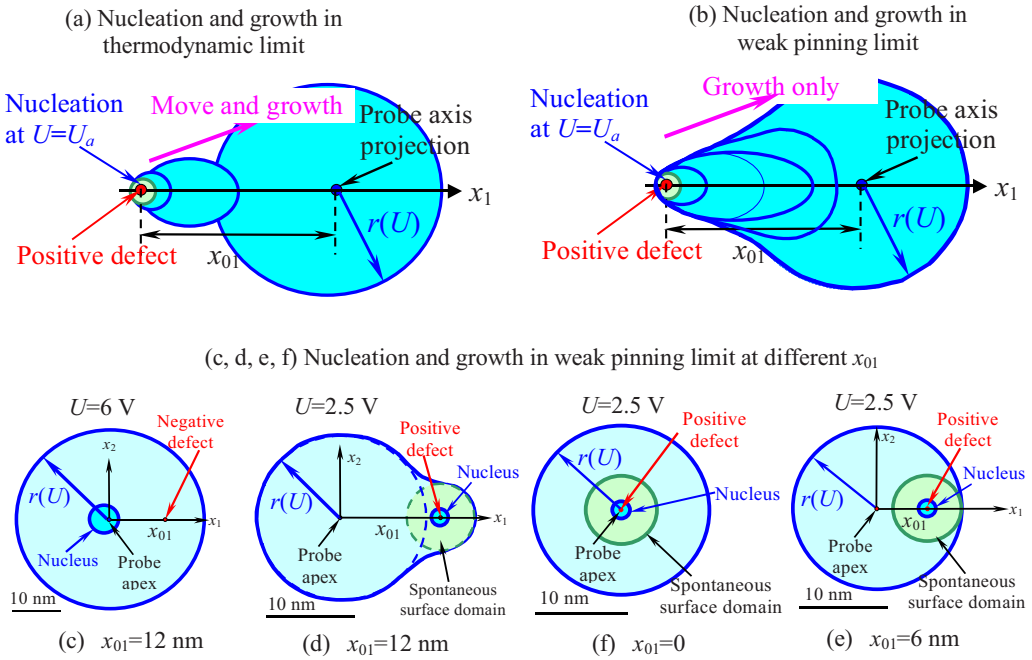

FIG. 6. (Color online) Sketch of domain nucleation, and growth in (a) thermodynamic limit and (b) weak pinning limit. [(c)–(f)] Calculated domain nucleation and growth in weak pinning limit at different x_{01}. Nucleus sizes are enlarged; $r(U)$ is equilibrium domain size at voltage U. Material parameters and tip characteristics are the same as in Fig. 5.

To describe the nucleus position analytically, we performed minimization on y_0 of the free energy Eq. (15) under the conditions $r<2d$ and $l\leq 2\gamma d$, typically valid in a saddle points, and derived in Appendix B the set of approximate expressions for the shift y_0 at $x_{01}\neq 0$:

$$y_0(U) = \begin{cases} \dfrac{x_S E_S \exp(-x_{01}^2/r_d^2)}{E_S \exp(-x_{01}^2/r_d^2) + U r_d^2 (d+h_d)/2d^3 h_d}, & UE_S > 0 \\ \dfrac{2\gamma d^3 h_d x_{01}}{r_d^2 (d+h_d)} \dfrac{E_S}{U} \exp\left[-\left(2\gamma \dfrac{d^3}{r_d^2} \dfrac{E_S}{U} - 1 \right)^2 \dfrac{x_{01}^2}{r_d^2} \right], & UE_S < 0 \end{cases} \tag{18}$$

Equation (18) qualitatively describes the behavior depicted in Fig. 5 including the cases of nucleus repulsion ($y_0<0$) at $E_S<0$ and attraction ($y_0>0$) at $E_S>0$, as well as $y_0\to 0$ at $x_{01}\gg r_d$. As anticipated, $y_0\to 0$ at high voltages. For the stable domains with sizes $l\gg r$ and $l\gg h_d$, we obtained that $y_0\approx 0$ for all voltages $U>\gamma|E_S|d^2h_d/r_d^2$. At $x_{01}=0$ and biases $0<U<-2\sqrt{2}\,\gamma E_S d^3 h_d/r_d^2(d+h_d)$, the (nonuniversal) ring-structure of radius $r_d\sqrt{\ln[-2\sqrt{2}\,\gamma E_S d^3 h_d/Ur_d^2(d+h_d)]}$ is most probable.

B. Activation barrier, critical voltage, and domain sizes

For a favorable field defect ($E_S<0$), domain nucleation can be either activationless at high enough built-in field or the activation barrier is lowered compared to ideal material, rendering the process feasible at lower biases. For an unfavorable field defect ($E_S>0$) or its absence ($E_S=0$), the domain formation process is always characterized by the activation energy, E_a, determined as the free-energy value in the saddle point. Minimization of the free energy [Eq. (15)] on the nucleus sizes r and l leads to the estimation of the activation barrier $E_a(U)$:

$$E_a(U) = \frac{2\pi\psi_S^3}{3}\left\{ \frac{3P_S d\cdot U}{\gamma[\sqrt{d^2+y_0^2}+d]^2} - \frac{P_S^2}{3\varepsilon_0\varepsilon_{11}} + \frac{3}{2}P_S E_S \exp\left[-\frac{(x_{01}-y_0)^2}{r_d^2} \right] F(h_d) \right\}^{-2}. \tag{19}$$

Here the function $F(h_d)\cong\exp(-9\varepsilon_0\psi_S/8h_dP_S^2)$. Corresponding nucleus sizes are $l_S(U)\sim r_S(U)\cong\sqrt{3E_a(U)/2\pi\psi_S}$, at that typically $r<2d$ and $l<2d$.

Activation voltages $U_a^0(E_S=0)$ and $U_a^{\pm}(E_S\neq 0)$, corresponding to different polarization sign $\pm P_S$ (or, equivalently, forward and reverse switchings), can be determined numerically from the free energy [Eq. (15)] using the conditions $\Phi(U_a^0, E_S=0, \pm P_S, l_S, r_S)=E_a$ and $\Phi(U_a^{\pm}, E_S, \pm P_S, l_S, r_S)=E_a$, or estimated analytically from Eq. (19). The following expressions were derived for the defect-free case:

$$U_a^0 \cong \pm\frac{4}{3}\gamma d\left(\sqrt{\frac{2\pi\psi_S^3}{3E_aP_S^2}} + \frac{|P_S|}{3\varepsilon_0\varepsilon_{11}} \right), \tag{20a}$$

and for defect-mediated switching:

$$U_a^{\pm} \cong \pm\frac{\gamma}{3d}(\sqrt{d^2+y_0^2}+d)^2\left(\sqrt{\frac{2\pi\psi_S^3}{3E_aP_S^2}} + \frac{|P_S|}{3\varepsilon_0\varepsilon_{11}} \right) - \Delta U(E_S), \tag{20b}$$

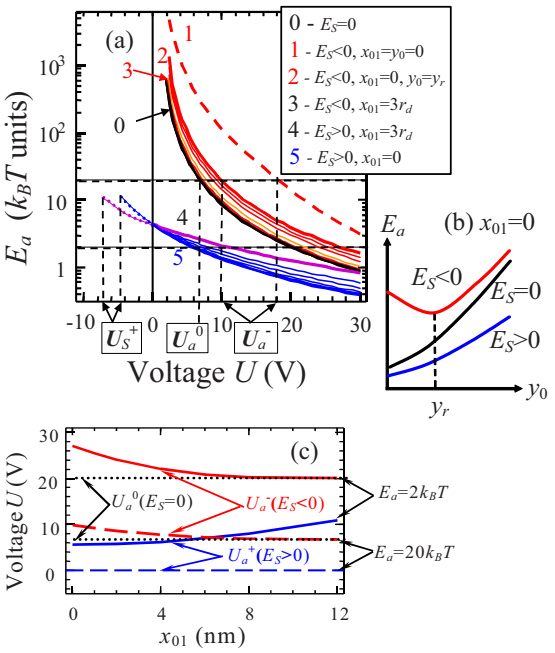

FIG. 7. (Color online) (a) Dependence of the energy barrier (in k_BT units) on the applied voltage U for surface field defect of r_d =4 and h_d=0.8 nm, and field strength E_S located at position x_{01}. Curve 0 corresponds to E_S=0. Curve 1 corresponds to the saddle y_0=0 [corresponding to the highest barrier, see schematics (b) for $E_a(y_0)$] at E_S=−10^9 V/m and x_{01}=0. Curve 2 corresponds to the saddle y_0=y_r≠0 [corresponding to the lowest barrier, see schematics (c) for $E_a(y_0)$] at E_S=−10^9 V/m and x_{01}=0. Curve 3 is calculated at E_S=−10^9 V/m and x_{01}=3r_d. Curve 4 is calculated at E_S =+10^9 V/m and x_{01}=3r_d. Curve 5 is calculated at E_S= +10^9 V/m and x_{01}=0. Intermediate thin curves are calculated at x_{01}=2r_d, 1.5r_d, r_d, and 0.5r_d nm, correspondingly. (c) Dependence of the activation voltage U_a at level 2 and 20k_BT on the distance to defect center, x_{01}. PZT-6B material parameters and tip characteristics are the same as in Fig. 3.

$$\Delta U(E_S) = \frac{\gamma}{2d}(\sqrt{d^2 + y_0^2} + d)^2 E_S \exp\left[-\frac{(x_{01} - y_0)^2}{r_d^2}\right] F(h_d). \tag{20c}$$

Here E_a is the potential barrier height chosen as a condition for thermally induced nucleation, e.g., 2k_BT–20k_BT. The lateral domain nucleus shift y_0 could be estimated from Eq. (18) self-consistently.

From the analysis above, the effect of defect on the hysteresis loop shape can be predicted as follows. In the presence of a defect, the hysteresis loop is broadened by the factor $(\sqrt{1+y_0^2/d^2}+1)^2-4$ compared to the defect-free case [see Eq. (20b)] due to the change in nucleation biases. Furthermore, the loop is shifted along the voltage axis by the value ΔU due to domain-defect interactions. The value ΔU exponentially decreases with the distance $|x_{01}-y_0|$ from the defect center.

For a favorable field defect ($E_S>0$), the domain nucleation with $P_S>0$ is characterized by the smaller activation voltages, U_a^+, or can even be spontaneous [i.e., U_a^+=0 because $E_a(0)<2k_BT$] at some values of x_{01} and E_S. This corresponds to the case when the surface state already exists at zero voltage and a certain negative voltage U_S^+ is required to destroy it. Voltage dependence of the domain activation energy E_a is shown in Fig. 7(a). Dependences of activation voltages $U_a^{0,\pm}$ (at levels 2k_BT and 20k_BT) on the distance x_{01} from the defect center are depicted in Fig. 7(c).

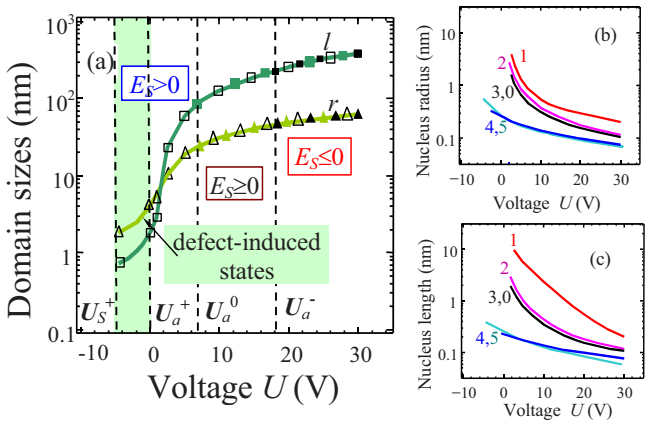

FIG. 8. (Color online) (a) Equilibrium domain radius r and length l dependence on the applied voltage for different surface field E_S: E_S=+10^9 V/m (empty symbols), E_S=0 (color symbols), and E_S=−10^9 V/m (black symbols). (b) and (c) Voltage dependence of nucleus sizes in a saddle point. Curves 0–5 correspond to the same E_S and x_{01} values as described in Fig. 7. PZT-6B material parameters, defect, and tip characteristics are the same as in Fig. 3.

For a material with PZT-6B parameters, the activation barrier may be extremely low in the vicinity of the positive surface field defect with field strength $E_S>10^8$ V/m. Curves 4 and 5 demonstrate that the surface state disappears at $U_S^+\approx-5$ V. For a negative surface field defect, no surface state exists and the activation barrier drastically increases, as follows from curves 1 and 2. For defects with equal absolute field strength, the role of positive defect in facilitating nucleation is much more long-range than a negative one. This reflects the fact that domain has much more preferential directions away from the defect than toward the defect.

Similar analysis for the reversed domain nucleation with $P_S<0$ affected by a negative surface field $E_S<0$ requires the introduction of voltage U_S^-, corresponding to the surface-state disappearance (U_a^-=0 is possible).

We compare the influence of the defect field and location on the voltage dependence of equilibrium domain and nucleus sizes in Fig. 8.

From Fig. 7(a), the equilibrium domain sizes are insensitive to the defect position and the field strength at the chosen material parameters. Only the positions of the origins of the curves (corresponding to activation voltage $U_a^{-,0}$ or U_S^+) are sensitive to the defect characteristics. The reason for this behavior is the condition $U_a^- \gg U_{cr}^-$ ($U_a^- \gtrsim 20$ V and $U_{cr}^- \lesssim 3$ V). The critical voltage U_{cr} depends on the defect characteristics but it governs the thermodynamic domain formation only at a close activation barrier $U_a \sim U_{cr}$. At voltages $U \gg U_{cr}$, domain growth becomes almost independent of the initial critical point. In contrast, the bias dependence of nucleus sizes is sensitive to the surface field defect, as demonstrated in Figs. 8(b) and 8(c). This analysis suggests that

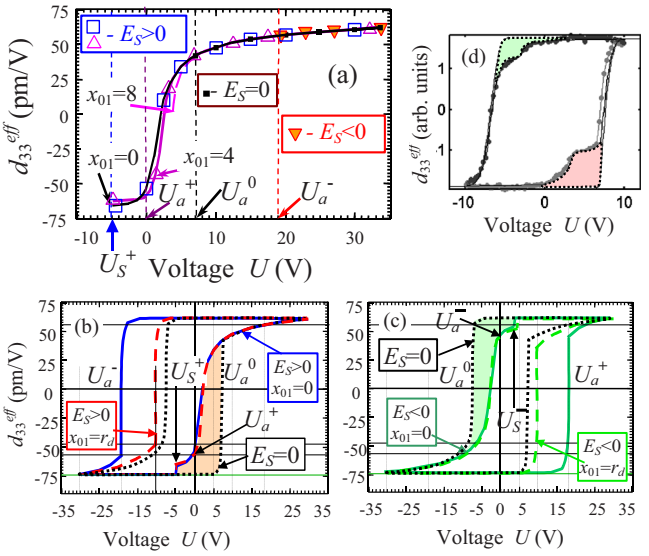

FIG. 9. (Color online) (a) Dependence of normalized PFM response on the applied voltage affected by the surface field defect. (b) and (c) PFM response loops in the weak pinning limit at surface field amplitude (b) $E_S=0,+10^9$ V/m and (c) $E_S=0,-10^9$ V/m. Dotted ($E_S=0$), dashed ($x_{01}=r_d$ and $E_S\neq 0$), and solid ($x_{01}=0$, $E_S\neq 0$) curves are calculated for coercive biases U_a^0, $U_S^{\pm}$, and $U_a^{\pm}$, estimated for nucleation onset $E_a=20k_BT$. Piezoelectric coefficients $d_{15}=135.6$ pm/V, $d_{31}=-28.7$ pm/V, and $d_{33}=74.9$ pm/V are used. (d) Typical experimental PFM response loop with fine structure (filled regions) (Ref. 37).

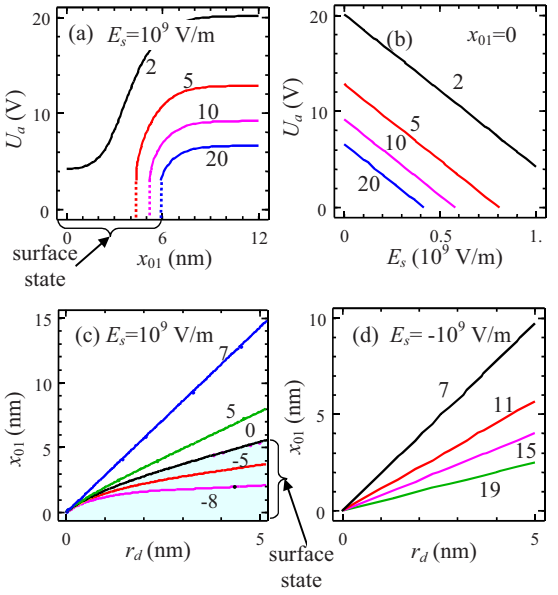

FIG. 10. (Color online) Dependence of activation voltage on (a) the distance x_{01} from the positive field defect (field strength $E_S=10^9$ V/m, $r_d=10$ nm, and $h_d=0.8$ nm) and (b) maximum defect field strength E_S for $x_{01}=0$ in PZT-6B for different values of activation energy E_a (figures near curves are E_a values in k_BT units). (c) and (d) Contour maps of U_a via the distance x_{01} and defect radius r_d at $E_A=20k_BT$ (figures near the curves are U_a values in V) for field strength (c) $E_S=10^9$ V/m and (d) $E_S=-10^9$ V/m. PZT-6B material parameters and tip characteristics are the same as in Fig. 3.

the primary influence of the surface field effect on the domain switching is the shift of activation energy (saddle point on free-energy surface) while equilibrium domain size is almost unaffected.

C. Effective piezoresponse and hysteresis loop fine structure

The effect of a surface field defect on the voltage dependence of the effective piezoresponse $d_{33}^{\text{eff}}[r(U)]$ calculated from Eqs. (9)–(11), (12a), and (12b) is shown in Fig. 9(a). Similarly to the behavior in Fig. 8(a), only the starting points of the piezoresponse curves (voltages U_a^0, $U_a^{\pm}$, or $U_S^{\pm}$) are sensitive to the defect characteristics. However, the change in the nucleation voltage defines piezoresponse loop fine structure and horizontal asymmetry, as shown in Figs. 9(b) and 9(c).

For the above scenario, the positive (PNB) and negative nucleation biases (NNB) can be written as $U_a^+=U_a^0-\Delta U$ and $U_a^-=-U_a^0-\Delta U$, correspondingly, where U_a^0 is the activation voltage that corresponds to defect-free nucleation [see symmetric dotted loops in Figs. 9(b) and 9(c)] and ΔU is described by Eq. (20c). The shift along the voltage axis is a direct effect of a defect influence. For $E_S>0$, the nucleation bias can be zero, $U_a^+=0$, as shown in Fig. 9(b). In this case, the piezoresponse loop exhibits fine structure at voltage U_S^+, i.e., a jumplike feature corresponding to a delayed nucleation [the filled region in Fig. 9(b)]. For a negative surface field, $E_S<0$, the piezoresponse loop fine structure appeared at voltage U_S^- and represents a bumplike feature corresponding to rapid switching within the defect [the filled region in Fig. 9(c)]. Such loop fine structure is often observed on experimental data,[37] as shown in Fig. 9(d).

Performed analysis proved that the presence of the localized surface field defects can strongly affect the structure of the hysteresis loop in PFM, inducing significant asymmetry and introducing reproducible fine-structure features. Thus, the analysis of the fine structure and its variation from point to point on the surface can potentially provide information on the density and strength of the defect, i.e., allowing the disorder potential to be reconstructed.

V. SURFACE STATE MAPS AND FINE-STRUCTURE LOOP DECONVOLUTION

The analysis of switching spectroscopy PFM (SS-PFM) three-dimensional (3D) data sets allows the characteristic parameters describing polarization switching such as work of switching (area within the loop), positive and negative nucleation biases, positive and remnant coercive biases, etc. to be plotted as 2D maps, correlating switching behavior with local topography. Characteristic feature of the field defect on the surface is the asymmetry of local nucleation bias. Illustrated in Fig. 10 are dependences of activation voltage on the distance from the defect, defect maximum field, and defect radius in PZT-6B.

The quantitative description of the piezoresponse loop $d_{33}^{\text{eff}}(U)$ fine structure requires several steps to be followed, including (i) tip shape calibration, (ii) deconvolution of the domain radius-voltage dependence $r(U)$, and (iii) analysis of

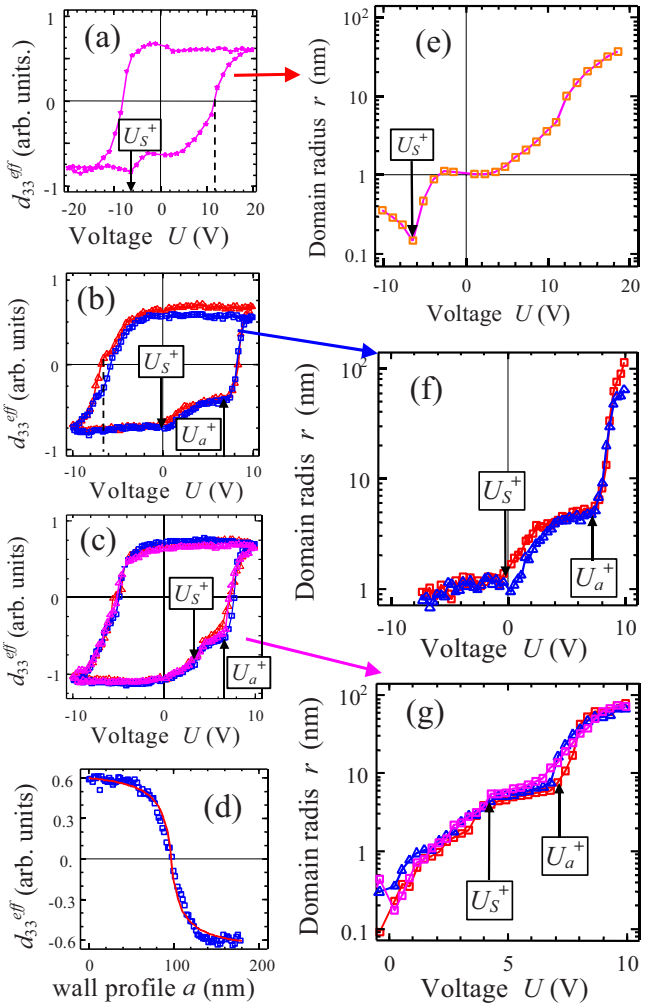

FIG. 11. (Color online) (a)–(c) Normalized PFM response loops in 200-nm-thick $BiFeO_3$ film with growth defects. (d) Tip calibration. Effective charge-surface separation d=6.9 nm was calculated within local point-charge model $d=\varepsilon_e R_0/\kappa$ at $BiFeO_3$ polarization P_S=0.5 C/m^2 with permittivity $\varepsilon_{11,33}=\kappa$=80. An ambient permittivity value ε_e=11 was obtained from the fitting of domain-wall profile (d) within the nominated tip curvature R_0=50 nm. (e)–(g) Voltage dependence of domain radius deconvoluted from (a)–(c). For deconvolution, the following parameters have been used: d_{33} =26 pm/V, d_{15}=3.5 pm/V, d_{31}=−12 pm/V, and γ=1 (Ref. 55).

defects energetics for a known set of $\{U_i, r_i\}$, where U_i is a voltage corresponding to ith fine feature and r_i corresponds to domain size.

Effective tip size (i.e., charge-surface distance d) can be determined self-consistently from the measured domain-wall width, as described in Ref. 54. With this information in hand, domain size deconvolution can be performed using an expression for $d_{33}^{\text{eff}}(r)$ given by Eq. (13), namely by extracting the dependence $r(U)$ from the experimentally measured $d_{33}^{\text{eff}}(U)$. From the experimentally observed hysteresis loop $d_{33}^{\text{eff}}(U)$ asymmetry and fine structure at different tip location with respect to the defect position x_{01}, one extracts defect characteristics such as surface field amplitude, E_S, and defect radius, r_d. Deconvolution of the 3D data set of ferroelectric hysteresis loops acquired at each point of the image represents a complex problem, generally amenable only to numerical algorithms. However, well-separated multiple field defects can be considered as a linear superposition of individual defects. Then generalizing analytical expressions [Eqs. (20)] for a distribution of Gaussian defects, deconvolution of the defect parameters from hysteresis loop nucleation bias and fine structure is possible as summarized below.

Typical deconvolution examples of $BiFeO_3$ hysteresis loops affected by growth defects are shown in Fig. 11. It is clear that U_S^+ values could be (a) negative, (b) approximately zero, or (c) positive. Description of experimental details can be found in Ref. 37.

Deconvolution of the 3D data set of ferroelectric hysteresis loops acquired at each point of the image represents a complex problem, generally amenable only to numerical algorithms. Using Eqs. (20), we derive a simplified analytical model for the deconvolution of the nucleation bias and fine-structure maps. For positive and negative nucleation bias maps for the case of nucleation below the tip, the nucleation biases are

$$U_{an}^{\pm} \cong \pm U_a^0 - 2\gamma d \sum_i \tilde{E}_{di}(x_{1n} - x_{01}^i, x_{2n} - x_{02}^i), \qquad (21)$$

where $n=1\ldots N$ is the number of scanning points, $\{x_{1n}, x_{2n}\}$ and $\{x_{01}^i, x_{02}^i\}$ are the center position of ith surface field defect, and $\tilde{E}_{di}(x_1, x_2)$ and $\{x_{1n}, x_{2n}\}$ are the domain center position that coincides with the tip apex location.

From Eq. (21) the defect-free nucleation bias

$$U_a^0 = \sum_n^N \frac{U_{an}^+ - U_{an}^-}{2N} \equiv \frac{4\gamma d}{3}\left(\sqrt{\frac{2\pi\psi_S^3}{3E_a P_S^2}} + \frac{|P_S|}{3\varepsilon_0\varepsilon_{11}}\right), \qquad (22)$$

and the bias difference (horizontal imprint bias)

$$\Delta U_{an} = U_{an}^+ + U_{an}^- = -4\gamma d \sum_i \tilde{E}_{di}(x_{1n} - x_{01}^i, x_{2n} - x_{02}^i). \qquad (23)$$

For purely surface field defects, Eq. (23) allows the reconstruction of the electric fields of the defect directly from the SS-PFM imprint map when separation d is determined from the probe calibration and the relevant basis for the resulting field $\Sigma_i \tilde{E}_{di}(x_1, x_2)$ expansion is chosen. For the Gaussian basis considered, the ith defect surface field is $\tilde{E}_{di}(x_1, x_2) = \tilde{E}_{Si} \exp[-(x_1^2 + x_2^2)/r_{di}^2]$, where $\tilde{E}_{Si} = E_{Si} F(h_{di})$ is the field amplitude.

The voltages corresponding to the fine-structure features are

$$U_{Sn}^+ \cong \frac{(\sqrt{d^2 + y_{0n}^2} + d)^2}{3d^2}\left[U_a^0 - 2\gamma d \sum_i \tilde{E}_{di}(y_{01}^n - x_{01}^i, y_{02}^n - x_{02}^i)\right], \qquad (24a)$$

and

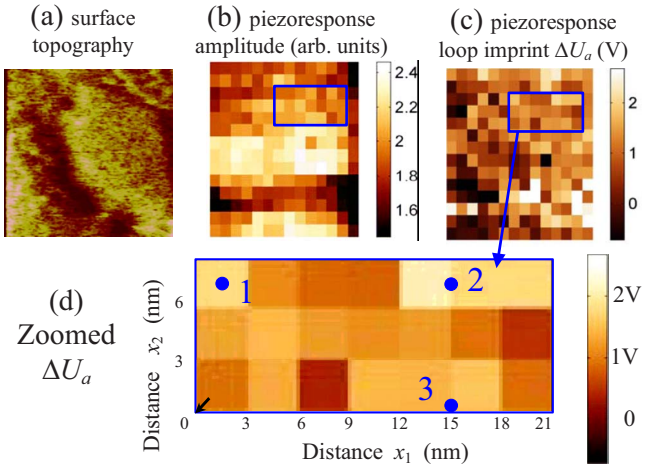

FIG. 12. (Color online) (a) Surface topography of 200-nm-thick $BiFeO_3$ film. (b) Local map of surface piezoresponse amplitude. (c) Local map of piezoresponse hysteresis loop imprint ΔU_a. (d) Zoomed imprint ΔU_{an} with defects 1, 2, and 3 positions marked by circles (experimental scanning results in cell coordinates). Cell size is about 3 nm.

$$U_{Sn}^{-} \cong -\frac{(\sqrt{d^2+y_{0n}^2}+d)^2}{3d^2}\left[U_a^0+2\gamma d\sum_i \tilde{E}_{di}(z_{01}^n-x_{01}^i,z_{02}^n-x_{02}^i)\right], \tag{24b}$$

where $\{y_{01}^n, y_{02}^n\}$ and $\{z_{01}^n, z_{02}^n\}$ are the domain center position that may differ from the tip apex location; $y_{0n}^2=(y_{01}^n)^2+(y_{01}^n)^2$ and $z_{0n}^2=(z_{01}^n)^2+(z_{01}^n)^2$.

In deconvolution of experimental data, nucleation and fine-structure biases $\{U_{an}^{-}, U_{an}^{+}, U_{Sn}^{-}, U_{Sn}^{+}\}$ in the scanning points $\{x_{1n}, x_{2n}\}$ are determined from hysteresis loops and could be presented as local maps [see Figs. 12(b)–12(d)].

At the first step, the fitting is performed with respect to the set of parameters $\{x_{01}^i, x_{02}^i, \tilde{E}_{Si}, r_{di}\}$ determined using Gaussian fits from the imprint biases $\{\Delta U_{an}\}$ in the points $\{x_{1n}, x_{2n}\}$. The amount of defects (i.e., the number of basis elements) depends on the necessary accuracy of surface field reconstruction.

At the second step, the domain center positions $\{y_{01}^n, y_{02}^n\}$ and $\{z_{01}^n, z_{02}^n\}$ are determined from the fine-structure biases maps $\{U_{Sn}^{-}, U_{Sn}^{+},\}$ using Gaussian fits. The data in Fig. 12(d) can be fitted using a model of six well-separated weak defects, or three strong defects, as demonstrated below. Using experimental loops in a 200 nm $BiFeO_3$ film, partially shown in Fig. 10, we have found that $U_a^0 \cong 5.5 \pm 0.3$ V and so $\psi_S = 104$ mJ/m^2 in accordance with Eq. (22). The loop shapes are determined by three short-ranged negative defects: the first one "1" with field amplitude $\tilde{E}_{S1}=-800$ kV/cm and radius $r_{di}=6$ nm located at coordinates {1.5 nm, 7.5 nm}; the second one "2" with $\tilde{E}_{S2}=-900$ kV/cm and $r_{d2}=2$ nm located at cell coordinates {15.5 nm, 7.5 nm}, and the third one "3" with $\tilde{E}_{S3}=-700$ kV/cm and $r_{d3}=3$ nm located at cell coordinates {15 nm, 0 nm}. Clearly, further progress necessitates the development of more efficient numerical algorithms for 3D data interpretation.

VI. CONCLUSIONS

The thermodynamics of bias-induced phase transition in ferroelectric material in the presence of well-localized surface field defects is analyzed, providing the extension of Landauer-Molotskii phenomenology. We demonstrate that well-localized field defect significantly affects the activation energy and nucleation bias of domain formation, and derived corresponding closed-form analytical expressions. Depending on the relative sign of the defect field and tip potential, the defect can impede or facilitate the nucleation, resulting in significant asymmetry of the hysteresis loop in piezoresponse force microscopy. For the case of well-localized defects, the equilibrium domain size is not affected by the defect strength at high voltages while the nucleation voltage required for switching is controlled by the defect, giving rise to universality of switching behavior.

The domain-defect interaction results in the reproducible fine structure of the hysteresis loops, somewhat similar to the force-distance curves in force-based atomic force microscopy. The presence of a reproducible fine feature is indicative of the finite defect size since extended defects (much larger than tip size) will result in uniform shift of hysteresis loop along the voltage axis. Correspondingly, fine feature variations in SS-PFM maps are predicted to be strongly correlated with nucleation bias distributions. This behavior is found to be in good agreement with experimental data on model $Pb(Zr,Ti)O_3$ and $BiFeO_3$ materials. The approach for the deconvolution of the hysteresis loop fine structure and analysis of the defect parameters has been demonstrated.

Presented analysis performed for local polarization switching can be similarly extended to other voltage induced phase transitions, including amorphization-crystallization in phase change memories, bias-induced metal-insulator transitions, and electrochemical reactions. For electromechanically active materials such as ferroelectrics and multiferroics, biopolymers, and biological systems, the detection method can be based on local electromechanical response. The combination of scanning probe microscopy with *in situ* electron microscopy will allow correlation of defect-mediated thermodynamics and kinetics of phase transitions with atomic structure, paving the pathway for understanding the atomistic mechanisms of switching.

ACKNOWLEDGMENTS

Research was sponsored in part (S.J., B.J.R., and S.V.K.) by the Division of Materials Sciences and Engineering, Office of Basic Energy Sciences, U.S. Department of Energy with Oak Ridge National Laboratory, managed and operated by UT-Battelle, LLC. A.N.M., E.A.E., and S.V.S. gratefully acknowledge financial support from National Academy of Science of Ukraine Grant No. N 13-07, joint Russian-Ukrainian Grant No. NASU N 17-Ukr_a (RFBR N 08-02-90434), Ministry of Science and Education of Ukraine Grant

No. N GP/F26/042, and CNMS at Oak Ridge National Laboratory.

APPENDIX A: FIELD DEFECT CHARGE-DENSITY DETERMINATION

We define the coordinate system with the origin at the defect center $\{x_{01},0,0\}$ and use the cylindrical coordinate system $\{\rho,\varphi,z\}$. The bulk charge density $\sigma_d(\rho,z)$ induced by the axisymmetric field defect with a given z component of the electric field, $E_z^S(\rho,z)$, can be found from the system of electrostatic Maxwell equations $rot\mathbf{E}^S=0$ and $\varepsilon_0\,\mathrm{div}(\hat{\varepsilon}\mathbf{E}^S)=\sigma_d$. In cylindrical coordinates $\{\rho,\phi,z\}$, we obtain

$$\frac{\partial}{\partial z}E_\rho^S(\rho,z)=\frac{\partial}{\partial \rho}E_z^S(\rho,z),\quad E_\rho^S(\rho,z)=\int^z\frac{\partial}{\partial \rho}E_z^S(\rho,z')dz', \tag{A1}$$

$$\sigma_d(\rho,z)=\varepsilon_0\left\{\frac{\varepsilon_{11}}{\rho}\frac{\partial}{\partial\rho}[\rho E_\rho^S(\rho,z)]+\varepsilon_{33}\frac{\partial}{\partial z}E_z^S(\rho,z)\right\}. \tag{A2}$$

Equation (A1) should be supplemented with relevant boundary conditions. For the perfect electric contact between the conductive tip and surface, $E_\rho^S(\rho,z=0)=0$ and $-\varepsilon_{33}\varepsilon_0E_3^S(\rho,z=0)=\sigma_b(\rho)$. The same model was used for depolarization and interaction energy calculations [e.g., Eq. (15)]. The free charge density $\sigma_b(\rho)$ is located inside the screening layer, or flattened tip apex or top electrode. Further derivation depends on the expression for $E_z^S(\rho,z)$. Z component of the electric field is

$$E_3^S(x,y,z)=E_S\exp\left[-\frac{(x-x_{01})^2+y^2}{r_d^2}-\frac{z}{h_d}\right]. \tag{A3}$$

Corresponding defect charge density is

$$\sigma_d(x,y,z)=-\varepsilon_0E_3^S(x,y,z)\frac{\varepsilon_{33}r_d^4+4\varepsilon_{11}[\exp(z/h_d)-1]h_d^2[r_d^2-(x-x_{01})^2-y^2]}{h_dr_d^4}. \tag{A4}$$

The charge density is maximal near the surface and rapidly decreases with depth, z. However it tends to constant value at $z\to\infty$, namely

$$\sigma_S(x,y,\infty)=-4\varepsilon_0\varepsilon_{11}E_S\exp\left[-\frac{(x-x_{01})^2+y^2}{r_d^2}\right][r_d^2-(x-x_{01})^2-y^2]\frac{h_d}{r_d^4}. \tag{A5}$$

Thus Eq. (A4) describes a continuous distribution resembling that of a charged dislocation line, in agreement with analysis in Ref. 53.

The dimensionless overlap integral $I_S(r,l,x)$ in Eq. (16) has the form

$$\begin{aligned}I_S(r,l,x)&=2\int_0^{l/h_d}dzf(z)\exp(-z)\int_0^{r/r_d}\rho d\rho\cdot I_0\left(2\frac{x}{r_d}\rho\right)\exp\left(-\rho^2-\frac{x^2}{r_d^2}\right)\\&\approx\left[1-\exp\left(-\frac{l}{h_d}\right)\right]\times\left[1-\exp\left(-\frac{r^2}{r_d^2}\right)\right]\exp\left(-\frac{x^2}{r_d^2}\right).\end{aligned} \tag{A6}$$

APPENDIX B: APPROXIMATE ANALYTICAL ANALYSES

1. Saddle point

To obtain approximate analytical results, we simplify the free energy [Eq. (15)] under the conditions $r<2d$ and $l<2\gamma d$, typically valid at nucleation stage (i.e., in a saddle point).

For $l<h_d$ and $r<r_d$, the free-energy [Eqs. (15) and (16)] Pade approximation becomes

$$\Phi\approx f_Sr^2S_D(\xi)+f_Dr^3N_D(\xi)+(f_U+f_d)r^3/\xi. \tag{B1a}$$

Note that Eq. (B1a) is valid at $d<h_d$ (since $r_d\gg h_d$).

For $r\gg r_d$ and $l\gg h_d$, it acquires the form

$$\Phi\approx f_Sr^2S_D(\xi)+f_Dr^3N_D(\xi)+f_Ur^3/\xi+f_dh_dr_d^2. \tag{B1b}$$

In Eqs. (B1) the domain aspect ratio $\xi=r/l$ determines the shape-function $S_D(\xi)=1+(\arcsin\eta)/\xi$ and depolarization factor $N_D(\xi)=\xi\gamma^2/1-\xi^2\gamma^2(\operatorname{arctanh}\eta/\eta-1)$, where $\eta=\sqrt{1-\xi^2}$, varying within the range $\{0,1\}$ in SI units. The characteristic energies are $f_S=\pi\psi_S$, $f_D=4\pi P_S^2/3\varepsilon_0\varepsilon_{11}$, $f_U(U)=-4\pi P_SdU/\gamma(\sqrt{d^2+y_0^2}+d)^2$, and $f_d=-2\pi P_SE_S\times\exp[-(x_{01}-y_0)^2/r_d^2]$. The nucleus center shift y_0 should satisfy transcendental equation $d(f_U+f_d)/dy_0=0$.

Minimization of Eq. (B1a) on the variables r and ξ leads to the parametric dependences on ξ of domain radius r, length l, and activation energy E_a:

$$r(U)=\frac{-2f_S\xi S_D(\xi)}{3[f_U+f_d+f_D\xi N_D(\xi)]}, \tag{B2a}$$

$$l(U)=\frac{-2f_SS_D(\xi)}{3[f_U+f_d+f_D\xi N_D(\xi)]}, \tag{B2b}$$

and

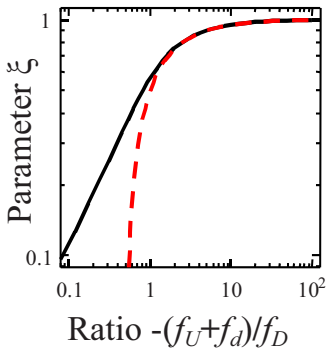

FIG. 13. (Color online) Parameter ξ via the ratio $-(f_U+f_d)/f_D$. Solid curve is exact solution and dashed curve is approximation $\xi \approx 1+f_D/2(f_U+f_d)$.

$$E_a(U) = \frac{-4f_S^3\xi^2 S_D(\xi)^3}{27[f_U+f_d+f_D\xi N_D(\xi)]^2}. \tag{B2c}$$

Transcendental equation for the parameter ξ has the form:

$$\xi^2\frac{2S_D(\xi)[dN_D(\xi)/d\xi]-3N_D(\xi)[dS_D(\xi)/d\xi]}{2S_D(\xi)+3\xi[dS_D(\xi)/d\xi]} = \frac{f_U+f_d}{f_D}. \tag{B3}$$

At $\xi\to 1$ denominator $2S_D(\xi)+3\xi(dS_D(\xi)/d\xi)$ tends to zero so that for the case of high biases $-(f_U+f_d)\gg f_D$, one can obtain approximate expressions for ξ. For the corresponding $S_D(\xi)$ and $N_D(\xi)$, the asymptotic representation is $\xi\approx 1+f_D/2(f_U+f_d)$ (see Fig. 13).

The expression along Eq. (B2) leads to

$$r(U) \approx \frac{-4f_S}{3(f_U+f_d)+f_D}, \tag{B4a}$$

$$l(U) \approx \frac{-4f_S}{3(f_U+f_d)+f_D}\left[1-\frac{f_D}{2(f_U+f_d)}\right], \tag{B4b}$$

and

$$E_a(U) \approx \frac{32(f_S)^3}{3[3(f_U+f_d)+f_D]^2}. \tag{B4c}$$

The Eqs. (B2)–(B4) are valid for $l\le h_d$ and $r\le r_d$ (by definition $r_d\gg h_d$).

Consideration of the free energy [Eq. (B2)–(B4)] valid in the opposite case, $l\gg h_d$ and $r\gg r_d$ leads to the same functional dependencies [Eqs. (B3)], where $f_U+f_d\to f_U$. Taking into account that the overlap integral [Eq. (16)] derivatives on l exponentially vanish as $\exp(-l/h_d)$ with domain length increase and the critical nucleus length, estimated under the condition $f_U+f_d>-f_D$, is about $1.5(f_S/f_D)$, expressions, particularly cases $l\le h_d$ and $l\gg h_d$, can be joined by substitution $f_d\to f_d\exp(-3f_S/2f_Dh_d)$. Thus, substituting the characteristic energies in Eq. (B4) yields

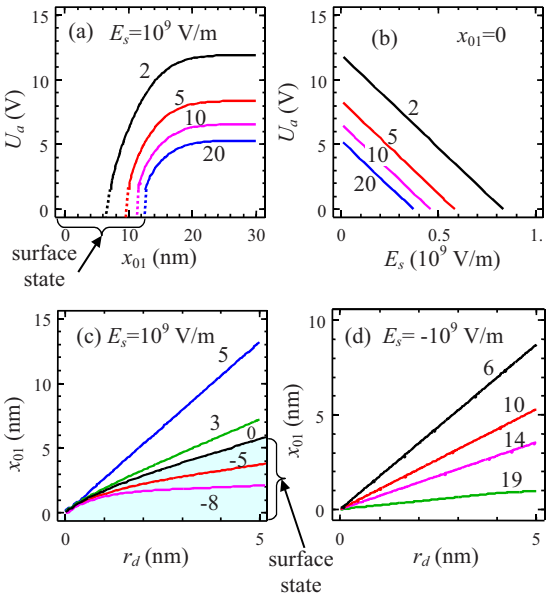

FIG. 14. (Color online) Dependence of activation voltage U_a on (a) the distance x_{01} from the positive field defect (field strength $E_S=10^9$ V/m, $r_d=10$ nm, and $h_d=0.8$ nm) and (b) maximum defect field strength E_S for $x_{01}=0$ in $BiFeO_3$ for different values of activation energy E_a (figures near curves are E_a values in k_BT units). (c) and (d) Contour maps of U_a via the distance x_{01}, and defect radius r_d at $E_a=20k_BT$ (figures near the curves are U_a values in V) for field strength (c) $E_S=10^9$ V/m and (d) $E_S=-10^9$ V/m. Material parameters correspond to a tetragonal $BiFeO_3$: $P_S=0.5$ C/m^2, $\varepsilon_{11}\approx\varepsilon_{33}\approx 80$, $\gamma\approx 1$, and $\psi_S=100$ mJ/m^2. Point-charge-surface separation $d=7$ nm.

$$r_S(U) \approx \psi_S\left\{\frac{3P_S d\cdot U}{\gamma[\sqrt{d^2+y_0^2}+d]^2}-\frac{P_S^2}{3\varepsilon_0\varepsilon_{11}} + \frac{3}{2}P_SE_S\exp\left[-\frac{(x_{01}-y_0)^2}{r_d^2}\right]F(h_d)\right\}^{-1}, \tag{B5a}$$

$$l_S(U) \approx r_S\left\{1+\frac{P_S}{3\varepsilon_0\varepsilon_{11}}\left[\frac{2dU}{\gamma(\sqrt{d^2+y_0^2}+d)^2} + E_S\exp\left[-\frac{(x_{01}-y_0)^2}{r_d^2}\right]F(h_d)\right]^{-1}\right\}, \tag{B5b}$$

and

$$E_a(U) \approx \frac{2\pi\psi_S^3}{3}\left\{\frac{3P_S d\cdot U}{\gamma(\sqrt{d^2+y_0^2}+d)^2}-\frac{P_S^2}{3\varepsilon_0\varepsilon_{11}} + \frac{3}{2}P_SE_S\exp\left[-\frac{(x_{01}-y_0)^2}{r_d^2}\right]F(h_d)\right\}^{-2}. \tag{B5c}$$

Here the function $F(h_d)=\exp(-9\varepsilon_0\psi_S/8h_dP_S^2)$, where the thickness $\varepsilon_0\psi_S/P_S^2$ is proportional to the intrinsic domain-wall width, of the order of several lattice constants. It reflects

the fact that the critical domain sizes cannot be smaller than the width.

2. Domain center shift

Minimization of the free energy [Eq. (B1a)] on y_0 leads to the transcendental equations:

$$y_0(U) = \frac{x_{01}E_S \exp[-(x_{01}-y_0)^2/r_d^2]}{E_S[-(x_{01}-y_0)^2/r_d^2] + 4Ur_d^2 d/\gamma(\sqrt{d^2+y_0^2}+d)^3\sqrt{d^2+y_0^2}}. \tag{B6a}$$

Equation (B6a) can be rewritten as

$$\frac{y_0-x_{01}}{r_d}\exp\left[-\left(\frac{y_0-x_{01}}{r_d}\right)^2\right] = \frac{-4Ur_d y_0 d}{E_S\gamma(\sqrt{d^2+y_0^2}+d)^3\sqrt{d^2+y_0^2}}. \tag{B6b}$$

In special case $x_{01}=0$, Eqs. (B6)give two possibilities: $y_0=0$ for $E_S U>0$ and the special point $y_0=y_r\neq 0$, corresponding to the divergence of denominator and existing at $E_S U<0$, namely:

$$y_r = \pm r_d\sqrt{\ln\left[-\frac{\gamma E_S\sqrt{d^2+y_r^2}}{4Ur_d^2 d}(\sqrt{d^2+y_r^2}+d)^3\right]} \approx \pm r_d\sqrt{\ln\left(-2\sqrt{2}\gamma\frac{E_S d^3}{Ur_d^2}\right)}. \tag{B7}$$

When the denominator in Eq. (B6a) is finite, it includes the cases $y_0<0$ at $UE_S<0$ and $y_0>0$ at $UE_S>0$. So, under the condition $x_{01}\neq 0$, approximate expression for the shift $y_0(U,r_S,l_S)$ is

$$y_0 \approx \begin{cases} \dfrac{x_{01}E_S\exp(-x_{01}^2/r_d^2)}{E_S\exp(-x_{01}^2/r_d^2)+Ur_d^2/2\gamma d^3}, & E_S U>0 \\ 2\gamma\dfrac{d^3}{r_d^2}\dfrac{x_{01}}{U}E_S\exp\left[-\left(2\gamma\dfrac{d^3}{r_d^2}\dfrac{E_S}{U}-1\right)^2\dfrac{x_{01}^2}{r_d^2}\right], & E_S U<0 \end{cases} \tag{B8}$$

Note that Eqs. (B7) and (B8) are derived for the case $l<h_d$ and $l<\gamma d$. Also we consider the case $l\gg h_d$, $l\gg\gamma d$, and obtained after elementary transformations:

$$y_r \approx \pm r_d\sqrt{\ln\left(-2\sqrt{2}\gamma\frac{E_S d^2 h_d}{Ur_d^2}\right)}. \tag{B9}$$

Under the condition $x_{01}\neq 0$ and $E_S>0$,

$$y_0 \approx \frac{x_{01}E_S\exp(-x_{01}^2/r_d^2)}{E_S\exp(-x_{01}^2/r_d^2)+Ur_d^2/2d^2h_d} \tag{B10}$$

Expressions (B8) and (B10) can be joined together in the sense of Pade approximation, as proposed in the main text [see Eq. (18)].

The kinetic instability corresponding to the switching between these two saddles ($y_0=0$ and $y_0=y_r$) is possible while in thermodynamic limit, the one corresponding to the lowest activation energy is realized.

3. Surface state critical field

From symmetry considerations, $x_{01}=y_0$ under the absence of external voltage U. For the case, numerical simulations proved that spontaneous (i.e., activationless) domain appearance is possible at $P_S E_S>0$. At $U=0$, the free energy is $f_S S_D(\xi)r^2+f_D N_D(\xi)r^3+f_d h_d r_d^2[1-\exp(-r^2/r_d^2)][1-\exp(-r/\xi h_d)]$. Typically, the spontaneous domain appears with sizes $l\leq h_d$, $r\leq r_d$, and $l<r$ (since $h_d\ll r_d$) if the built-in field is more than the critical value: $E_S^{cr}\approx(2/3)(\psi_S/h_d P_S+P_S/\varepsilon_0\varepsilon_{11})$. More rigorous estimation of the critical built-in field of surface-state appearance leads to

$$E_S^{cr}\cong\frac{2e}{3(e-1)}\left(\frac{\psi_S}{h_d P_S}+\frac{P_S}{\varepsilon_0\varepsilon_{11}}\right). \tag{B11}$$

The voltage of the saddle-point appearance (preceding to the critical point or surface-state origin) could be estimated from Eq. (B5c) as $E_a\leq 2-20k_BT$, allowing for the condition $y_0\sim x_{01}$ at $U_S^{\pm}E_S<0$. Note, that the voltage could be negative, indicating the possibility of surface-state (meta)stability.

Under the condition $E_S>0$, the jump appeared at voltage $U_S^+<0$ ($U_a^+=0$) of surface domain state origin,

$$U_S^+\cong\frac{\gamma}{3d}(\sqrt{d^2+y_0^2}+d)^2\left\{\sqrt{\frac{2\pi\psi_S^3}{3E_a P_S^2}}+\frac{|P_S|}{3\varepsilon_0\varepsilon_{11}}-\frac{3}{2}E_S\exp\left[-\frac{(y_0-x_{01})^2}{r_d^2}\right]F(h_d)\right\}. \tag{B12a}$$

Under the condition $E_S<0$, the jump appeared at voltage $U_S^->0$ ($U_a^-=0$) of surface domain state appearance,

$$U_S^-\cong-\frac{\gamma}{3d}(\sqrt{d^2+y_0^2}+d)^2\left\{\sqrt{\frac{2\pi\psi_S^3}{3E_a P_S^2}}+\frac{|P_S|}{3\varepsilon_0\varepsilon_{11}}+\frac{3}{2}E_S\exp\left[-\frac{(y_0-x_{01})^2}{r_d^2}\right]F(h_d)\right\}. \tag{B12b}$$

Here E_a is the activation energy chosen as condition for thermally induced nucleation, e.g., $2k_BT-20k_BT$.

Illustrated in Fig. 14 are dependences of activation voltage on the distance from the defect, defect maximum field, and defect radius in $BiFeO_3$ of tetragonal symmetry.[55,56]

*Corresponding author. morozo@i.com.ua
†Corresponding author. sergei2@ornl.gov

[1] A. P. Levanyuk and A. S. Sigov, *Defects and Structural Phase Transitions* (Gordon and Breach, New York, 1988).
[2] A. S. Sidorkin, *Domain Structure in Ferroelectrics and Related Materials* (Cambridge International Science, Cambridge, 2006).
[3] V. Wadhawan, *Introduction to Ferroic Materials* (Cambridge University Press, Cambridge, 2000).
[4] *Nanoelectronics and Information Technology*, edited by R. Waser (Wiley, New York, 2005).
[5] J. F. Scott, *Ferroelectric Memories*, 1st ed. (Springer, New York, 2000).
[6] J. Rodríguez-Contreras, H. Kohlstedt, U. Poppe, R. Waser, C. Buchal, and N. A. Pertsev, Appl. Phys. Lett. **83**, 4595 (2003).
[7] A. Bune, S. Ducharme, V. M. Fridkin, L. Blinov, S. Plato, N. Petukhova, and S. Yudin, Appl. Phys. Lett. **67**, 3975 (1995).
[8] Y. Cho, J. Nanosci. Nanotechnol. **7**, 105 (2007).
[9] S. P. Alpay, I. B. Misirlioglu, V. Nagarajan, and R. Ramesh, Appl. Phys. Lett. **85**, 2044 (2004).
[10] V. Nagarajan, C. L. Jia, H. Kohlstedt, R. Waser, I. B. Misirlioglu, S. P. Alpay, and R. Ramesh, Appl. Phys. Lett. **86**, 192910 (2005).
[11] I. B. Misirlioglu, S. P. Alpay, M. Aindow, and V. Nagarajan, Appl. Phys. Lett. **88**, 102906 (2006).
[12] A. N. Kolmogorov, Bull. Acad. Sci. USSR, Math. Ser. **1**, 355 (1937).
[13] M. Avrami, J. Chem. Phys. **8**, 212 (1940).
[14] Y. Ishibashi and Y. Takagi, J. Phys. Soc. Jpn. **31**, 506 (1971).
[15] J. F. Scott, J. Phys.: Condens. Matter **18**, R361 (2006).
[16] T. Nattermann, Y. Shapir, and I. Vilfan, Phys. Rev. B **42**, 8577 (1990).
[17] R. Landauer, J. Appl. Phys. **28**, 227 (1957).
[18] R. Ahluwalia and W. Cao, Phys. Rev. B **63**, 012103 (2000).
[19] R. Ahluwalia and W. Cao, J. Appl. Phys. **93**, 537 (2003).
[20] A. M. Bratkovsky and A. P. Levanyuk, Phys. Rev. Lett. **85**, 4614 (2000).
[21] G. Gerra, A. K. Tagantsev, and N. Setter, Phys. Rev. Lett. **94**, 107602 (2005).
[22] A. Grigoriev, D. H. Do, D. M. Kim, C. B. Eom, B. Adams, E. M. Dufresne, and P. G. Evans, Phys. Rev. Lett. **96**, 187601 (2006).
[23] A. Gruverman, B. J. Rodriguez, C. Dehoff, J. D. Waldrep, A. I. Kingon, R. J. Nemanich, and J. S. Cross, Appl. Phys. Lett. **87**, 082902 (2005).
[24] D. J. Kim, J. Y. Jo, T. H. Kim, S. M. Yang, B. Chen, Y. S. Kim, and T. W. Noh, Appl. Phys. Lett. **91**, 132903 (2007).
[25] M. Molotskii, A. Agronin, P. Urenski, M. Shvebelman, G. Rosenman, and Y. Rosenwaks, Phys. Rev. Lett. **90**, 107601 (2003).
[26] M. Molotskii, J. Appl. Phys. **93**, 6234 (2003).
[27] A. N. Morozovska, E. A. Eliseev, and S. V. Kalinin, Appl. Phys. Lett. **89**, 192901 (2006).
[28] C. S. Ganpule, A. L. Roytburd, V. Nagarajan, B. K. Hill, S. B. Ogale, E. D. Williams, R. Ramesh, and J. F. Scott, Phys. Rev. B **65**, 014101 (2001).
[29] A. Roelofs, N. A. Pertsev, R. Waser, F. Schlaphof, L. M. Eng, C. Ganpule, V. Nagarajan, and R. Ramesh, Appl. Phys. Lett. **80**, 1424 (2002).
[30] A. Agronin, Y. Rosenwaks, and G. Rosenman, Appl. Phys. Lett. **88**, 072911 (2006).
[31] A. L. Kholkin, I. K. Bdikin, V. V. Shvartsman, A. Orlova, D. Kiselev, A. A. Bogomolov, and S. H. Kim, in *Scanning Probe and Other Novel Microscopies of Local Phenomena in Nanostructured Materials*, edited by S. V. Kalinin, B. Goldberg, L. M. Eng, and B. D. Huey, MRS Symposia Proceedings No. 838E (Materials Research Society, Warrendale, PA, 2005), O7.6.
[32] J. Woo, S. Hong, N. Setter, H. Shin, J. U. Jeon, Y. E. Pak, and K. No, J. Vac. Sci. Technol. B **19**, 818 (2001).
[33] V. V. Shvartsman and A. L. Kholkin, J. Appl. Phys. **101**, 064108 (2007).
[34] V. Likodimos, M. Labardi, X. K. Orlik, L. Pardi, M. Allegrini, S. Emonin, and O. Marti, Phys. Rev. B **63**, 064104 (2001).
[35] V. Likodimos, M. Labardi, and M. Allegrini, Phys. Rev. B **66**, 024104 (2002).
[36] G. Le Rhun, I. Vrejoiu, L. Pintilie, D. Hesse, M. Alexe, and U. Gösele, Nanotechnology **17**, 3154 (2006).
[37] S. Jesse, B. J. Rodriguez, S. Choudhury, A. P. Baddorf, I. Vrejoiu, D. Hesse, M. Alexe, E. A. Eliseev, A. N. Morozovska, J. Zhang, L.-Q. Chen, and S. V. Kalinin, Nat. Mater. **7**, 209 (2008).
[38] S. V. Kalinin, S. Jesse, B. J. Rodriguez, Y. H. Chu, R. Ramesh, E. A. Eliseev, and A. N. Morozovska, Phys. Rev. Lett. **100**, 155703 (2008).
[39] M. Abplanalp, J. Fousek, and P. Günter, Phys. Rev. Lett. **86**, 5799 (2001).
[40] C. Harnagea, A. Pignolet, M. Alexe, D. Hesse, and U. Gösele, Appl. Phys. A: Mater. Sci. Process. **70**, 261 (2000).
[41] S. Buhlmann, Ph.D. thesis, EPFL, 2003.
[42] G. Le Rhun, I. Vrejoiu, and M. Alexe, Appl. Phys. Lett. **90**, 012908 (2007).
[43] S. Jesse, H. N. Lee, and S. V. Kalinin, Rev. Sci. Instrum. **77**, 073702 (2006).
[44] S. Jesse, A. P. Baddorf, and S. V. Kalinin, Appl. Phys. Lett. **88**, 062908 (2006).
[45] L. D. Landau and E. M. Lifshitz, *Electrodynamics of Continuous Media* (Butterworth Heinemann, Oxford, UK, 1980).
[46] A. N. Morozovska, S. V. Svechnikov, E. A. Eliseev, and S. V. Kalinin, Phys. Rev. B **76**, 054123 (2007).
[47] D. A. Scrymgeour and V. Gopalan, Phys. Rev. B **72**, 024103 (2005).
[48] E. A. Eliseev, S. V. Kalinin, S. Jesse, S. L. Bravina, and A. N. Morozovska, J. Appl. Phys. **102**, 014109 (2007).
[49] A. N. Morozovska, E. A. Eliseev, S. L. Bravina, and S. V. Kalinin, Phys. Rev. B **75**, 174109 (2007).
[50] F. Felten, G. A. Schneider, J. Muñoz Saldaña, and S. V. Kalinin, J. Appl. Phys. **96**, 563 (2004).
[51] L. D. Landau and E. M. Lifshitz, *Theory of Elasticity*, Theoretical Physics Vol. 7 (Butterworth-Heinemann, Oxford, UK, 1998).
[52] S. V. Kalinin, E. A. Eliseev, and A. N. Morozovska, Appl. Phys. Lett. **88**, 232904 (2006).
[53] C. Shi, P. M. Asbeck, and E. T. Yu, Appl. Phys. Lett. **74**, 573 (1999).
[54] S. V. Kalinin, S. Jesse, B. J. Rodriguez, E. A. Eliseev, V. Go-

palan, and A. N. Morozovska, Appl. Phys. Lett. **90**, 212905 (2007).

[55] A. N. Morozovska, E. A. Eliseev, and S. V. Kalinin, J. Appl. Phys. **102**, 074105 (2007).

[56] J. Wang, J. B. Neaton, H. Zheng, V. Nagarajan, S. B. Ogale, B. Liu, D. Viehland, V. Vaithyanathan, D. G. Schlom, U. V. Waghmare, N. A. Spaldin, K. M. Rabe, M. Wuttig, and R. Ramesh, Science **299**, 1719 (2003).